第37卷第6期
2018年12月

红外与毫米波学报
J. Infrared Millim. Waves

Vol. 37, No. 6
December, 2018

文章编号: 1001-9014(2018)06-0717-06

DOI: 10.11972/j.issn.1001-9014.2018.06.014

Design and imaging demonstrations of a terahertz quasi-optical Schottky diode detector

LI Ming-Xun[1], MOU Jin-Chao[2*], GUO Da-Lu[1], QIAO Hai-Dong[1], MA Zhao-Hui[1], LYU Xin[1]

(1. Beijing Key Laboratory of Millimeter Wave and Terahertz Technology, School of Information and Electronics, Beijing Institute of Technology, Beijing 100081, China;
2. Aerospace Long March Launch Vehicle Technology CO., LTD., Beijing 100094, China)

Abstract: A terahertz quasi-optical detector has been presented, which is mainly composed of a GaAs antenna-coupled Schottky diode chip and a highly resistive silicon lens. In order to reduce the ohmic loss, the standard terahertz Schottky diode fabrication process has been improved by forming the antenna patterns on the semi-insulating GaAs layer. Experimental responsivity and DSB conversion loss of the quasi-optical detector are 1360 ~ 1650 V/W and 10.6 ~ 12.5 dB at 335 ~ 350 GHz range, respectively. The noise equivalent power (NEP) is estimated to be 1.65 ~2 pW/Hz$^{1/2}$. Imaging experiments based on this quasi-optical detector have been carried out in both direct- and heterodyne-detection modes, successfully demonstrating its potential in terahertz imaging applications.

Key words: terahertz quasi-optical detector, direct detection, heterodyne detection, terahertz imaging
PACS: 07.57.Kp

基于肖特基二极管的太赫兹准光探测器设计方法与成像性能研究

李明迅[1], 牟进超[2*], 郭大路[1], 乔海东[1], 马朝辉[1], 吕 昕[1]
(1. 北京理工大学 信息与电子学院 毫米波太赫兹北京市重点实验室,北京 100081;
2. 航天长征火箭技术有限公司,北京 100094)

摘要:设计了一款太赫兹准光探测器,该探测器主要由砷化镓肖特基二极管芯片以及高阻硅透镜组成.为了减小所设计芯片的欧姆损耗,将天线图案生长在了半绝缘砷化镓层上.在335~350 GHz频率范围内,准光探测器的实测电压响应率为1360~1650 V/W,双边带变频损耗为10.6~12.5 dB.对应估算的等效噪声功率为1.65~2 pW/Hz$^{1/2}$.基于所设计的准光探测器进行了成像实验,该实验分别在直接检波和外差探测两种模式间进行,成像结果表明所设计的太赫兹准光探测器能够满足太赫兹成像方面应用.

关 键 词:太赫兹准光探测器;直接检波;外差探测;太赫兹成像
中图分类号:TN454 **文献标识码**:A

Introduction

Quasi-optical detector has long been used in many terahertz applications such as body security screening[1-3], non-destructive testing[4], biological sensing[5] and chemical analysis[6]. Instead of the metal waveguide cavity, quasi-optical detector usually use a lens to feed energy to the detector. Based on this space-feed structure, quasi-optical detector can operate flexibly in either direct- or heterodyne-detection mode, which provides an alternative receiving scheme. In addition to this, quasi-optical detector is able to achieve a wider bandwidth compared with the traditional waveguide-based detectors[7], and easy to extend to an array without the fabrication of the metal waveguide.

The current quasi-optical detectors used in terahertz applications include Schottky barrier diode (SBD), field effect transistor (FET), high electron mobility transistor (HEMT), bolometer, micro and nanobolometer[8-10]. A-

Received date: 2018-03-16, **revised date**: 2018-08-24 **收稿日期**:2018-03-16, **修回日期**:2018-08-24
Foundation items: Supported by the Special Fund for Basic Research on Scientific Instruments of the National Natural Science Foundation of China (61527805)
Biography: LI Ming-Xun (1990-), male, Hebei China. Ph. D. Research area involves terahertz device and terahertz imaging. E-mail: lmxxbit@163.com
* **Corresponding author**: E-mail: moujinchao@live.com

mong these devices, Schottky barrier diodes has been the preferred detector over the past decades and still play an important role in terahertz imaging applications for their excellent sensitivity, high speed and fabrication simplicity at room temperature[9-10].

In this paper, we design an antenna-coupled Schottky diode chip on GaAs substrate. The chip has been packaged into a quasi-optical detector with a highly-resistive silicon lens at 340 GHz. In order to reduce the ohmic loss, the standard terahertz Schottky diode fabrication process has been improved by forming the antenna patterns on the semi-insulating (S. I.) GaAs layer. Characterizations and imaging performance of the detector are experimentally measured and analyzed. Results show its potential in terahertz imaging applications.

1 Design of the quasi-optical detector

Figure 1(a) presents the configuration of the quasi-optical Schottky diode detector. It consists of a GaAs antenna-coupled Schottky diode chip, a highly-resistive silicon lens, a low-frequency PCB and a SMA connector. All the above components are packaged in a copper holder with a cover on the bottom, as shown in Fig. 1(b). The lens is stably fixed into the holder by a rubber ring and the chip is wire-bonded onto the LF-PCB. THz signal will incident into the lens and received by the antenna-coupled chip. Output low-frequency signal will be read out through the SMA connector. Figure 1(c) shows photograph of the assembled quasi-optical detector.

1.1 Antenna-coupled Schottky diode chip

Figure 2 (a) shows the GaAs antenna-coupled Schottky diode chip, with the dimension of 600 μm (width) ×800 μm (length) ×35 μm (thickness). It consists of a differentially-fed antenna on chip with a planar Schottky diode embedded across its central terminals. The real 3D view of the chip obtained by a non-contact confocal interferometry 3D profiler is given in Fig. 2 (b). The positive polarity of the Schottky diode is connected to the left wing of the antenna by an air bridge while its negative polarity is in direct connection with the right wing of the antenna. Two pads locate at the ends of the antenna, facilitating wire-bonding onto the LF-PCB. Here, a classical wideband planar log-periodic antenna (LPA) is employed in our design.

Figure 2(c) illustrates the vertical structure of the chip. The substrate is S. I. GaAs with a thickness of 35 μm. A highly-doped n^+-GaAs layer and a lowly-doped n^--GaAs layer are stacked on the S. I. GaAs substrate in succession. The Schottky contact formed by sputtering Ti/Pt/Au on the n^--GaAs layer. A surface channel is etched to provide isolation between the two wings of the antenna on chip. An air bridge suspending above the channel will connect the Schottky junction to the left wing of the antenna. A light and extremely thin passivation layer based on SiO_2 will coat on the chip after the formation of the Schottky junction and antenna patterns, ensuring the chip be less affected or corroded by the environment of future use. The two pad areas at the ends are exposed without coating for wire-bonding. To reduce ohmic loss in the chip, the antenna patterns are formed on the S. I. GaAs layer. In this case, the antenna patterns are easily broken because there will be a deep step between the surface of the N^--layer and the S. I. layer. As a result, we improve our standard terahertz Schottky diode chip technology, where two pairs of step are etched as shown in Fig. 5(c).

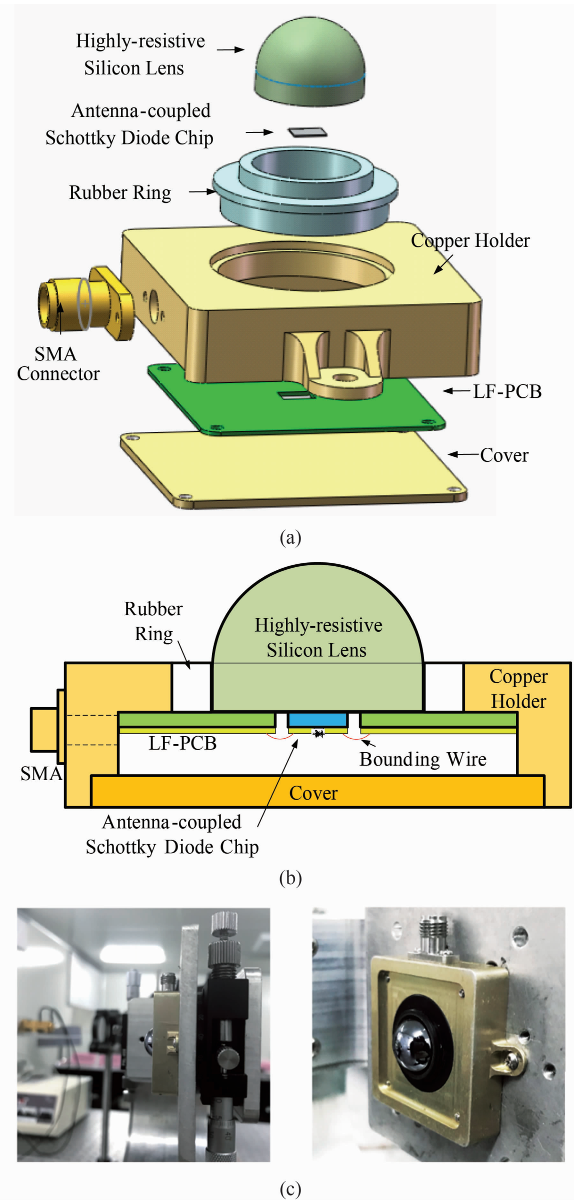

Fig. 1 Quasi-optical Schottky diode detector (a) perspective view, (b) cross sectional view, and (c) fabricated and assembled structure
图 1 准光肖特基二极管探测器 (a)透视图,(b)截面图,(c)装配结构

The Schottky junction is the key component that takes in charge of frequency conversion. There are three important factors that determine the performance of the Schottky junction. First, the doping concentration N_D^- and thickness t_{N-} of the N^--layer will determine the depletion region under the Schottky anode, which will directly affect the series resistance R_S and the ideality n of the Schottky diode. Second, the doping concentration

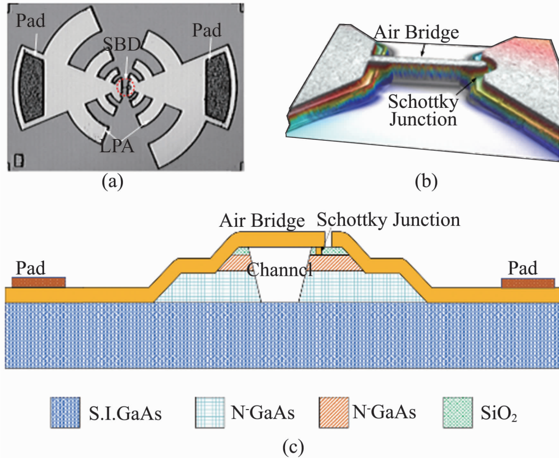

Fig. 2　(a) Photograph of the antenna-coupled Schottky diode chip under microscope, (b) 3D view near the Schottky junction region, obtained by a non-contact confocal interferometry 3D profiler, (c) vertical structure of the chip
图 2　(a)集成天线的肖特基二极管芯片显微照片,(b)肖特基结的三维轮廓仪照片,(c)芯片的垂直结构示意图

N_D^+ and thickness t_{N+} of the N^+-layer will determine the bulky resistance in the N^+-layer and the quality of the ohmic contact of the Schottky diode. Thus, they are related to R_S. Third, the anode will introduce junction capacitance C_j in the Schottky diode, where its diameter D_A is in direct proportion to C_j. Therefore, we optimize $\{N_D^-, t_{N-}, N_D^+, t_{N+}, D_A\}$ in order to obtain efficient detection at 340 GHz. Table 1 summarized the final optimized parameters.

Table 1　Parameters of GaAs epitaxial layers
表 1　砷化镓外延层参数

N_D^-	N_D^+	t_{N-}	t_{N+}	D_A
2E17 cm^{-3}	7E18 cm^{-3}	800 Å	3.5 μm	1 μm
DIODE'S	R_S	C_{j0}	n	I_S
PARAMETER	9.8 Ω	1.16 fF	1.24	1.78E-14 A

1.2　Highly-resistive silicon lens

As the thickness of the chip is only about 1/10 λ_d, the log-periodic antenna on chip shows bidirectional radiation patterns with low gain. In order to render the patterns unidirectional and enhance the gain, we load a highly-resistive silicon lens on the bottom of the chip. As silicon has a relative dielectric constant of $\varepsilon_r = 11.7$ which is close to that of GaAs ($\varepsilon_r = 12.9$), the wave impedance mismatching between the silicon lens and GaAs chip can be minimized.

Figure 3 shows the geometry of the silicon lens, consisting of a hemisphere with a radius R_1 and an extended cylinder with the same section radius and an extension length L_1. We choose 6.5 mm as R_1 for the purpose of ensuring the lens surface is located in the far field of the planar log-periodic antenna. By carefully optimizing L_1 using MLFMA algorithm refer to [11], the extension length determined as 2.75 mm with a simulated gain of 29.4 dBi at 340 GHz. Simulated and measured radiation patterns are compared in next section.

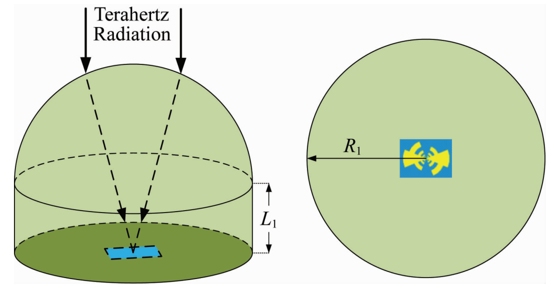

Fig. 3　Geometry of the silicon lens
图 3　硅透镜的几何结构

2　Experimental characterizations of the quasi-optical detector

The quasi-optical detector has been experimentally evaluated using the method in Ref. [12].

Firstly, we measured the radiation pattern of the lens-coupled antenna at 340 GHz. Simulated and measured results are plotted in Fig. 4. Due to the block of the copper holder, the back lobe of the lens could not be detected. Comparing the measured radiation patterns and the simulated ones, they show a good agreement in the main lobe. The difference in side lobe between the measured and simulated results are caused by the shield of the cooper holder and the rubber rings.

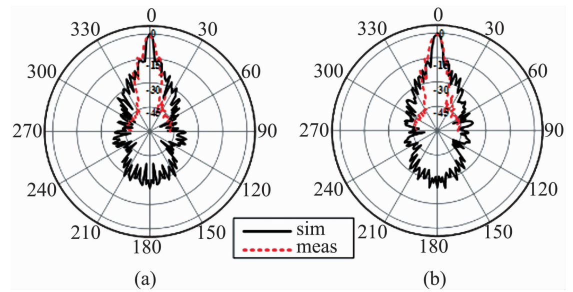

Fig. 4　Simulated and measured radiation patterns of the lens-coupled antenna at 340 GHz (a) E-plane radiation pattern, and (b) H-plane radiation pattern
图 4　340 GHz 频点下透镜天线的仿真与实测方向图(a) E 面方向图,(b) H 面方向图

Next, the responsivity in direct-detection mode and DSB conversion loss in heterodyne-detection mode of the quasi-optical detector are measured, respectively. As can be seen in Fig. 5, the quasi-optical detector shows a responsivity of 1 360 ~ 1 650 V/W and a conversion loss of 10.6 ~ 12.5 dB at 335 ~ 250 GHz range. Table 2 compares our detector with other designs based on Schottky diode, showing that our design has good performance in both modes.

Finally, the NEP of the quasi-optical detector can be calculated as

$$\mathrm{NEP} = \frac{\sqrt{4kTB(R_s + R_d)}}{R_V}$$

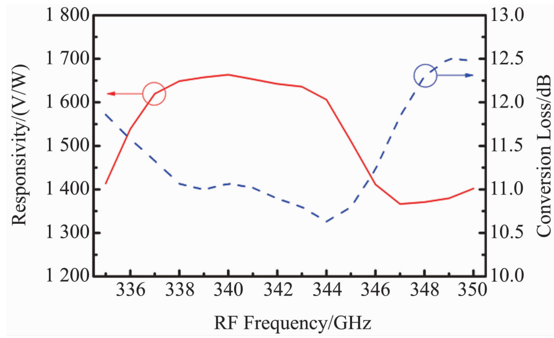

Fig. 5 Measured responsivity in direct-detection mode (red, solid) and DSB conversion loss in heterodyne mode (blue, dashed)
图 5 检波模式下测得的响应率(红色实线)和外差模式下测得的双边带变频损耗(蓝色虚线)

Table 2 Comparisons with other reported terahertz detectors
表 2 与其他报道的太赫兹探测器对比

Ref.	Freq. /GHz	Device	Res. [Direct] /(V/W)	DSB Conv. L [Heterodyne] /dB
[7]	150 ~ 400	GaAs ZBD	300 ~ 1 000	N. A.
[13]	1 ~ 110	InGaAs SRTD	1 200 ~ 1 600	N. A.
[14]	270 ~ 290	CMOS SBD	50 ~ 250	N. A.
[15]	300 ~ 1 200	InP SBD	125 ~ 1 000	N. A.
[16]	144 ~ 152	GaAs SBD	N. A.	11.5 ~ 12.5
[17]	86 ~ 106	GaAs SBD	N. A.	5.7 ~ 6.7
Our Work	335 ~ 350	GaAs SBD	1 360 ~ 1 650	10.6 ~ 12.5

The NEP is estimated to be 1.65 ~ 2 pW/Hz$^{1/2}$ based on the measured results.

3 Imaging demonstrations

3.1 Imaging system

An imaging system has been designed to demonstrate the imaging performance of our quasi-optical detector in direct- and heterodyne-detection modes. As shown in Fig. 6, four polytetrafluoroethylene (PTFE) plano-convex optical lenses (OL) and a silicon beam splitter (BS) are used for collecting and guiding the terahertz illumination. The quasi-optical detector is placed at the focus of OL#4 with a distance of 300 mm. The object under imaging is placed at the focus of OL#2 with a distance of 100 mm. It is fixed on a computer-controlled X-Y translation stage and moves following a meander line for two dimensionally spatial sampling. RF (f_{RF} = 340 GHz) and LO (f_{LO} = 338.6 GHz) sources are laid in face-to-face illumination, both of which are placed at the focus of their corresponding optical lenses with a distance of 100 mm, respectively. A Beam splitter is located at the center of this system in order to guide the illumination.

Both RF and LO sources are comprised by ×24 multiplication chains, providing a continuous output of 10 mW at room temperature. The IF read-out chain contains an IF amplifier (35 dB gain at 1.4 GHz) and a square law detector (1 000 V/W sensitivity at 1.4

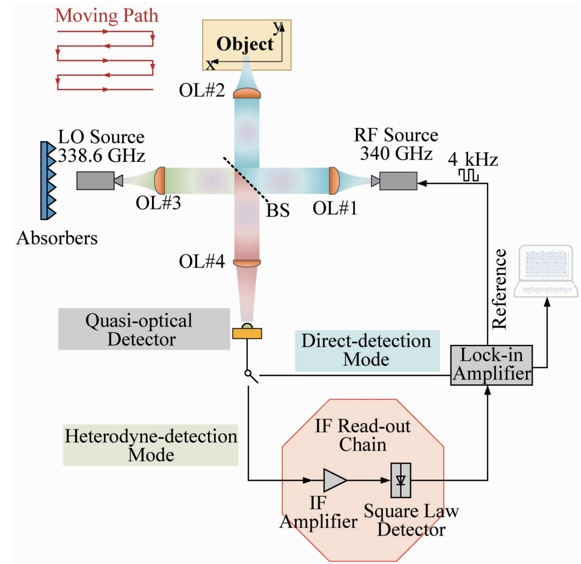

Fig. 6 Schematic diagram of the imaging system
图 6 成像系统原理图

GHz). The lock-in amplifier (SR-850) can provide a 4-kHz reference square wave for modulating the amplitude of RF signal and synchronously detect the based-band signal.

In direct-detection mode, the quasi-optical detector operates as a square law detector. The RF source illuminates on the object while the LO source holds OFF-state. The reflected RF radiation is detected by the quasi-optical detector and then read out by the lock-in amplifier. If switch to heterodyne-detection-mode, we should turn the switch to heterodyne-detection mode and turn on the LO source. The quasi-optical detector mixes the reflected RF radiation with the LO radiation and output the IF signal ($f_{IF} = |f_{RF} - f_{LO}|$). In this case, the quasi-optical detector actually plays a role as a mixer. After amplified and detected by the IF read-out chain, the output signal will also be readout by the lock-in amplifier. The recorded voltage in lock-in amplifier will be numerically mapping to a grey scale for imaging.

3.2 Imaging results

We perform the imaging experiments on a complex object as shown in Fig. 7(a). The objects contain a semicircular silicon wafer, a rectangular rubber sheet and a metallic key. During the imaging experiments, they will be fixed on the translation stage in stack as shown in Fig. 7(b). Several features of the object under imaging should be clarified. First, the silicon wafer's left part is gold-sputtered and right part keeps original, where the boundary A-A' is marked in Fig. 7(a). In this case, the silicon wafer presents different reflectivity and transmissivity in different regions. Second, a narrow crack orienting horizontally on the silicon wafer should be highlighted (Part B-B', Fig. 7(a)). The crack is difficult to be detected because the reflectivity between the crack and neighboring wafer is quite small, so it can be used to distinguish the sensitivity of the imaging results. Third, the metal key is arranged to evaluate the spatial resolution of the imaging system. Details of the key are dimensioned in Fig. 7(a). Forth, the rectangle rubber sheet

is used to fix the metal key and silicon wafer, also provide a reference for analyzing the system's spatial resolution.

To make a trade-off between the scanning speed and receiving S/N ration, the integration time of each pixel is 30 ms and scanning speed is 30 mm/s. In this case, the scan step satisfies the law of space sampling with a measurement bandwidth of 16.7 Hz. The total scanning region covers about 120 mm × 100 mm and the whole image contains 15000 pixels with a pixel pitch of 0.9 mm. Capturing one image takes about 7 minutes with a single-pixel quasi-optical detector.

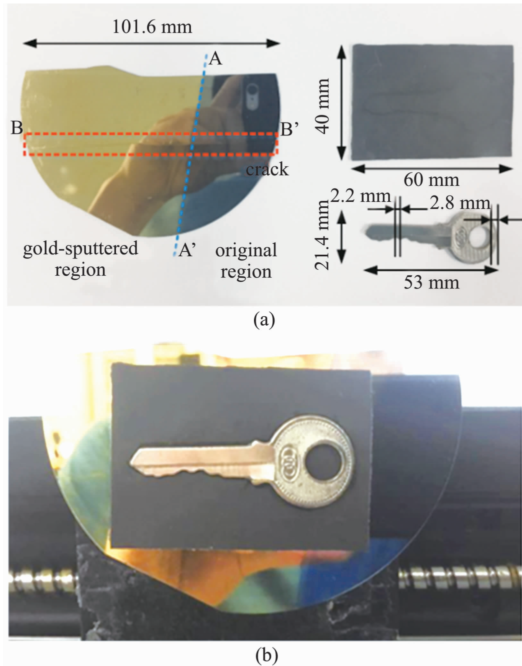

Fig. 7　Objects under imaging: (a) in separate arrangement, and (b) in stack

图 7　待测物体照片(a)分开放置,(b)堆叠放置

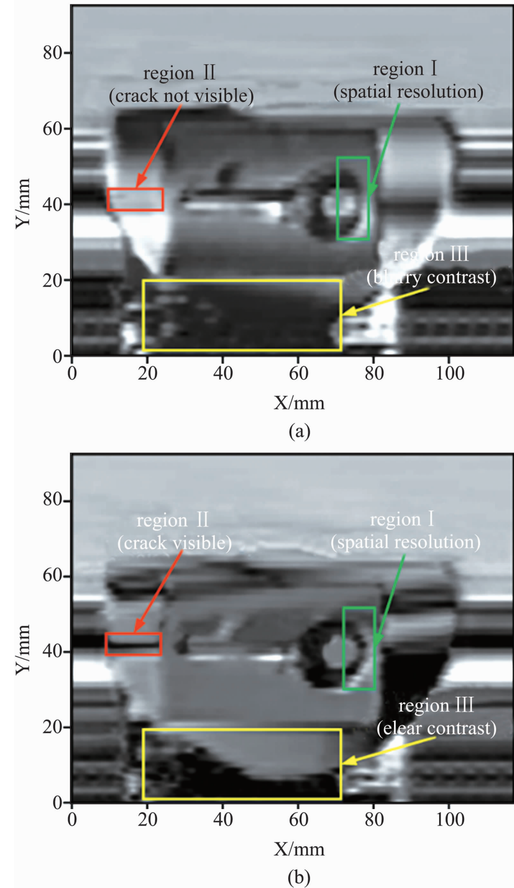

Fig. 8　Imaging results: (a) direct-detection mode and (b) heterodyne detection mdoe

图 8　成像结果(a)直接检波模式,(b)外差探测模式

Figure 8 shows the imaging results of the object, where the black pixel and white pixel correspond to the lowest and highest voltage, respectively. As shown in Figs. 8(a-b), all the items are clearly outlined in both detection modes. It may be mentioned that the edge between the right top of the circular through-hole and the key's handle is perfectly resolved (see region I in Figs. 8(a-b)), indicating that the spatial resolution of the system is not worse than 2.8 mm.

Comparing Fig. 8(a) with Fig. 8(b), we can find that the imaging result in heterodyne-detection mode exhibits a wider dynamic range and better sensitivity than the direct-detection mode. As we can see from region II in Figs. 8(a-b), the narrow crack in the silicon wafer is imaged only in heterodyne-detection mode. In addition to this, clear contrast between the lower edge of the silicon wafer and the translation stage is displayed in heterodyne-detection mode. But the same area is blurry in the direct-detection mode, as shown in region III from Fig. 8. Followings are the quantitatively evaluation on the performance of those two detection modes . The output voltage range of the imaging experiments is 0.098 ~ 3 mV in the direct-detection mode and 3.1 ~ 431 mV in heterodyne-detection mode. Therefore, the dynamic range of heterodyne-detection mode is 6.5 dB higher than direct-detection mode. Furthermore, by de-embedding the budget of the IF-readout chain, the minimum input power of the system is -41.8 dBm and -49.1 dBm in the direct- and heterodyne-detection modes, respectively. This means that the sensitivity of the system in the heterodyne-detection mode is 7.3 dB better than that in the direct-detection mode. The above analysis validates the imaging results shown in Fig. 8.

4　Conclusion

A terahertz quasi-optical detector has been designed and fabricated based on a GaAs antenna-coupled Schottky diode chip and a highly resistive silicon lens. Measured responsivity and DSB conversion loss at 335 ~ 350 GHz range are competitive compared with the list references. To demonstrate its imaging performance, we design an imaging system and perform an experiment in both direct- and heterodyne-detection modes. Imaging results show the potential of our quasi-optical detector in terahertz imaging applications.

References

[1] Appleby R, Wallace H B. Standoff detection of weapons and contraband in the 100 GHz to 1 THz region [J]. *IEEE Transactions on Antennas and Propagation*, 2007, **55**(11):2944-2956.

[2] Cooper K B, Dengler R J, Llombart N, *et al*. THz imaging radar for standoff personnel screening[J]. *IEEE Transactions on Terahertz Science and Technology*, 2011, **1**(1):169-182.

[3] Grajal J, Badolato A, Rubio-Cidre G, *et al*. 3-D High-resolution imaging radar at 300 GHz with enhanced FoV [J]. *IEEE Transactions on Microwave Theory and Techniques*, 2015, **63**(3):1097-1107.

[4] Shen Y C, Taday P F. Development and application of terahertz pulsed imaging for nondestructive inspection of pharmaceutical tablet [J]. *IEEE Journal of Selected Topics in Quantum Electronics*, 2008, **14**(2):407-415.

[5] Bowman T C, El-Shenawee M, Campbell L K. Terahertz imaging of excised breast tumor tissue on paraffin sections [J]. *IEEE Transactions on Antennas and Propagation*, 2015, **63**(5):2088-2097.

[6] Ajito K, Ueno Y. THz chemical imaging for biological applications [J]. *IEEE Transactions on Terahertz Science and Technology*, 2011, **1**(1):293-300.

[7] Liu L, Hesler J L, Xu H, *et al*. A broadband quasi-optical terahertz detector utilizing a zero bias schottky diode [J]. *IEEE Microwave and Wireless Components Letters*, 2010, **20**(9):504-506.

[8] Hadi R A, Sherry H, Grzyb J, *et al*. A 1 k-Pixel video camera for 0.7 ~ 1.1 terahertz imaging applications in 65-nm CMOS [J]. *IEEE Journal of Solid-State Circuits*, 2012, **47**(12):2999-3012.

[9] Liu L, Rahman S M, Jiang Z, *et al*. Advanced terahertz sensing and imaging systems based on integrated III-V interband tunneling devices [J]. *Proceedings of the IEEE*, 2017, PP(99):1-15.

[10] Sizov F, Rogalski A. THz detectors [J]. *Progress in Quantum Electronics*, 2010, **34**(5):278-347.

[11] Filipovic D F, Rebeiz G M. Double-slot antennas on extended hemispherical and elliptical quartz dielectric lenses [J]. *IEEE Transactions on Microwave Theory and Tech*, 1993, **41**(10):1905-1924.

[12] Daher C, Torres J, Iñiguez-De-La-Torre I, *et al*. Room temperature direct and heterodyne detection of 0.28 - 0.69-THz waves based on GaN 2-DEG unipolar nanochannels [J]. *IEEE Transactions on Electron Devices*, 2017, **63**(1):353-359.

[13] Chahal P, Morris F, Frazier G. Zero bias resonant tunnel Schottky contact diode for wide-band direct detection [J]. *IEEE Electron Device Letters*, 2005, **26**(12):894-896.

[14] Han R, Zhang Y, Coquillat D, *et al*. A 280-GHz Schottky diode detector in 130-nm digital CMOS [J]. *IEEE Journal of Solid-State Circuits*, 2011, **46**(11):2602-2612.

[15] Ito H, Nakajima F, Ohno T, *et al*. InP-based planar-antenna-integrated Schottky-barrier diode for millimeter- and sub-millimeter-wave detection [J]. *Japanese Journal of Applied Physics*, 2008, **47**(8):6256-6261.

[16] Gauthier G P, Raskin J P, Rebeiz G M. A 140-170-GHz low-noise uniplanar subharmonic Schottky receiver [J]. *IEEE Transactions on Microwave Theory and Techniques*, 2000, **48**(8):1416-1419.

[17] Ali-Ahmad W Y, Bishop W L, Crowe T W, *et al*. An 86-106 GHz quasi-integrated low noise Schottky receiver [J]. *IEEE Transactions on Microwave Theory and Techniques*, 1992, **41**(4):558-564.